Perforated Metal Oxide–Carbon Nanotube Composite Microspheres with Enhanced Lithium-Ion Storage Properties

Seung Ho Choi, Jong-Heun Lee, and Yun Chan Kang*

Department of Materials Science and Engineering, Korea University, Anam-Dong, Seongbuk-Gu, Seoul 136-713, Republic of Korea

ABSTRACT Metal oxide–carbon nanotube (CNT) composite microspheres with a novel structure were fabricated using a one-step spray pyrolysis process. Metal oxide–CNT composite microspheres with a uniform distribution of void nanospheres were prepared from a colloidal spray solution containing CNTs, metal salts, and polystyrene (PS) nanobeads. Perforated SnO_2–CNT composite microspheres with a uniform distribution of void nanospheres showed excellent lithium storage properties as anode materials for lithium-ion batteries. Bare SnO_2 microspheres and SnO_2–CNT composite microspheres with perforated and filled structures had a discharge capacity of 450, 1108, and 590 mA h g^{-1} for the 250th cycle at a current density of 1.5 A g^{-1}, and the corresponding capacity retention compared to the second cycle was 41, 98, and 55%, respectively. The synergetic combination of void nanospheres and flexible CNTs improved the electrochemical properties of SnO_2. This effective and innovative strategy could be used for the preparation of perforated metal oxide–CNT composites with complex elemental compositions for many applications.

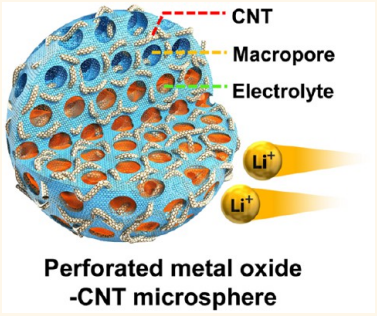

KEYWORDS: carbon nanotube · carbon composite · anode material · lithium-ion battery

Innovative design and synthesis of nanostructured materials have attracted much research interest for energy storage, including applications in lithium-ion batteries (LIBs).[1−12] In LIBs, the introduction of macropores in nanostructured materials has led to excellent electrochemical properties of the active material.[13−22] Macropores provide good channels for the penetration of the electrolyte into the nanostructured active material, thereby improving the electrochemical properties at high charge/discharge rates.[13−22] In addition, macropores supply voids to accommodate the huge volume change of the transition metal oxide during repeated lithium insertion and desertion.[13,19−24] However, the relatively low electrical conductivity of the macroporous metal oxide host limits the rate significantly. In general, only modest improvements in rate have been observed because macroporous structures primarily address ion transport and not electron transport.[18] Therefore, carbonaceous materials with high electrical conductivity and structural flexibility can improve the electrochemical properties of transition metal oxide materials with low electrical conductivities.[25−34]

Carbon nanotubes (CNTs) have high electrical conductivity and structural flexibility and have been used in composites with transition metal oxides.[34−37] Many studies have focused on the manufacture of irregularly shaped metal oxide–CNT composites by mechanical mixing or coating processes such as atomic layer deposition, chemical vapor deposition, and hydrothermal and precipitation processes.[34−55] CNT fiber-grafted metal oxide nanoparticles can not only serve as the backbone for the volume expansion of the electroactive materials during cycling but also facilitate electron/charge transfer in metal oxides.[34−55] Recently, metal oxide–CNT composite microspheres for LIBs have been prepared by spray pyrolysis using metal oxide nanoparticles and CNT fibers.[38] Microspheres with sizes of several microns could be used as anode materials in LIBs due to the formation of high-density electrode layers. However, to the best of our knowledge, the preparation of macroporous metal oxide–CNT composite microspheres

* Address correspondence to yckang@korea.ac.kr.

Received for review June 23, 2015 and accepted September 7, 2015.

Published online September 07, 2015
10.1021/acsnano.5b03822

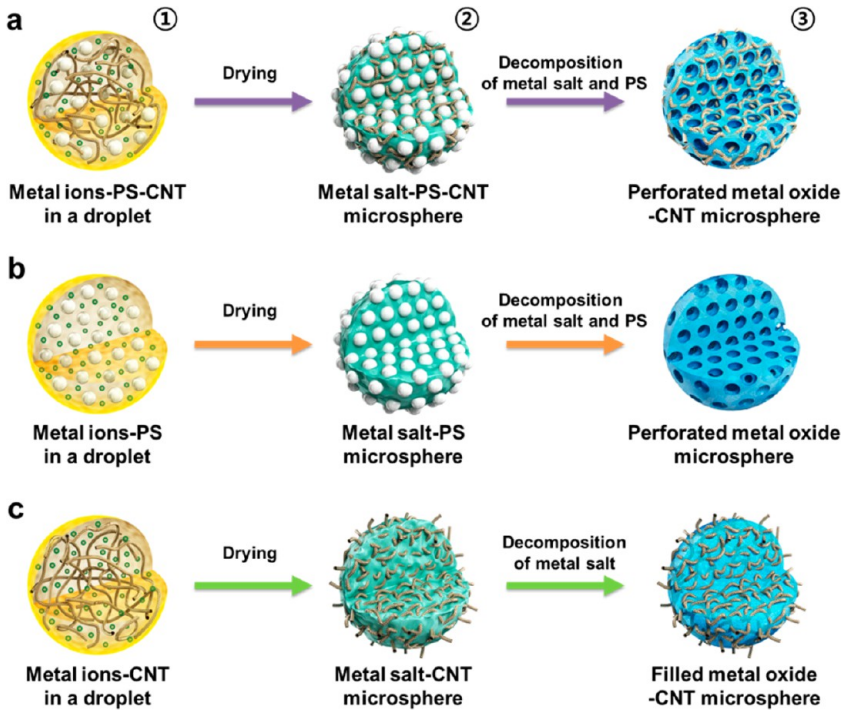

Scheme 1. Schematic diagram of the formation of microspheres by one-step spray pyrolysis: (a) perforated SnO_2–CNT composite, (b) bare SnO_2 microspheres with a uniform distribution of void nanospheres, and (c) filled SnO_2–CNT composite microsphere.

with a uniform distribution of void nanospheres and their application as anode materials for LIBs have not been reported.

Herein, a new design for metal oxide–CNT composite microspheres was successfully achieved in a one-step spray pyrolysis process (Figure S1). Metal oxide–CNT composite microspheres with a uniform distribution of void nanospheres were prepared from a colloidal spray solution containing CNTs, metal salts, and polystyrene (PS) nanobeads. PS nanobeads were applied as an organic template for the formation of void nanospheres within the metal oxide–CNT composite microspheres. In this study, SnO_2–CNT, NiO–CNT, WO_3–CNT, and GeO_2–CNT systems were successfully applied as the newly designed nanostructured materials. Metal oxide–CNT composite microspheres with a uniform distribution of void nanospheres showed excellent lithium storage properties as anode materials for LIBs. The synergetic combination of void nanospheres and flexible CNTs improved the electrochemical properties of the transition metal oxide. Our approach to fabricating macroporous metal oxide–CNT composite microspheres with a perforated structure may be valuable for widespread applications including energy storage.

RESULTS AND DISCUSSION

The formation of metal oxide–CNT composite microspheres with a uniform distribution of void nanospheres by one-step spray pyrolysis is described in Scheme 1. Droplets several microns in size containing CNTs, PS nanobeads, and metal salt were formed by the ultrasonic nebulizer (Scheme 1, ①). Oxygen functional groups, which formed on the surface of the CNTs by acid treatment, improved the dispersion stability of the spraying solution with CNTs.[56] Therefore, flexible CNTs were uniformly distributed within droplets. Tangled CNTs aggregated with a uniform distribution of PS nanobeads due to the network formed by flexible CNTs with a high aspect ratio as the droplets dried. Then, metal salt was deposited onto the three-dimensional CNT–PS network to form metal salt–CNT–PS composite microspheres with a filled structure (Scheme 1, ②). Thermal decomposition of the metal salt occurred completely at the rear part of the reactor that was maintained at 700 °C. At the same time, the PS nanobeads decomposed into CO_2 and water vapor in an argon atmosphere to produce void nanospheres uniformly dispersed in the metal oxide–CNT composite microspheres (Scheme 1, ③). The uniform exposure of PS nanobeads on the surface of the metal salt–CNT–PS composite microspheres, as shown in Scheme 1, ②, resulted in opened macropores in the metal oxide–CNT composite microspheres. In addition, the high volume fraction of PS nanobeads within the droplets resulted in connections between the nanobeads after the droplet dried. Therefore, burning the interconnected PS nanobeads led to the formation of nanoholes connecting the void nanospheres.[57,58] Thus, the metal oxide–CNT composite microspheres with a uniform distribution of void nanospheres had an ideal structure for electrolyte penetration into

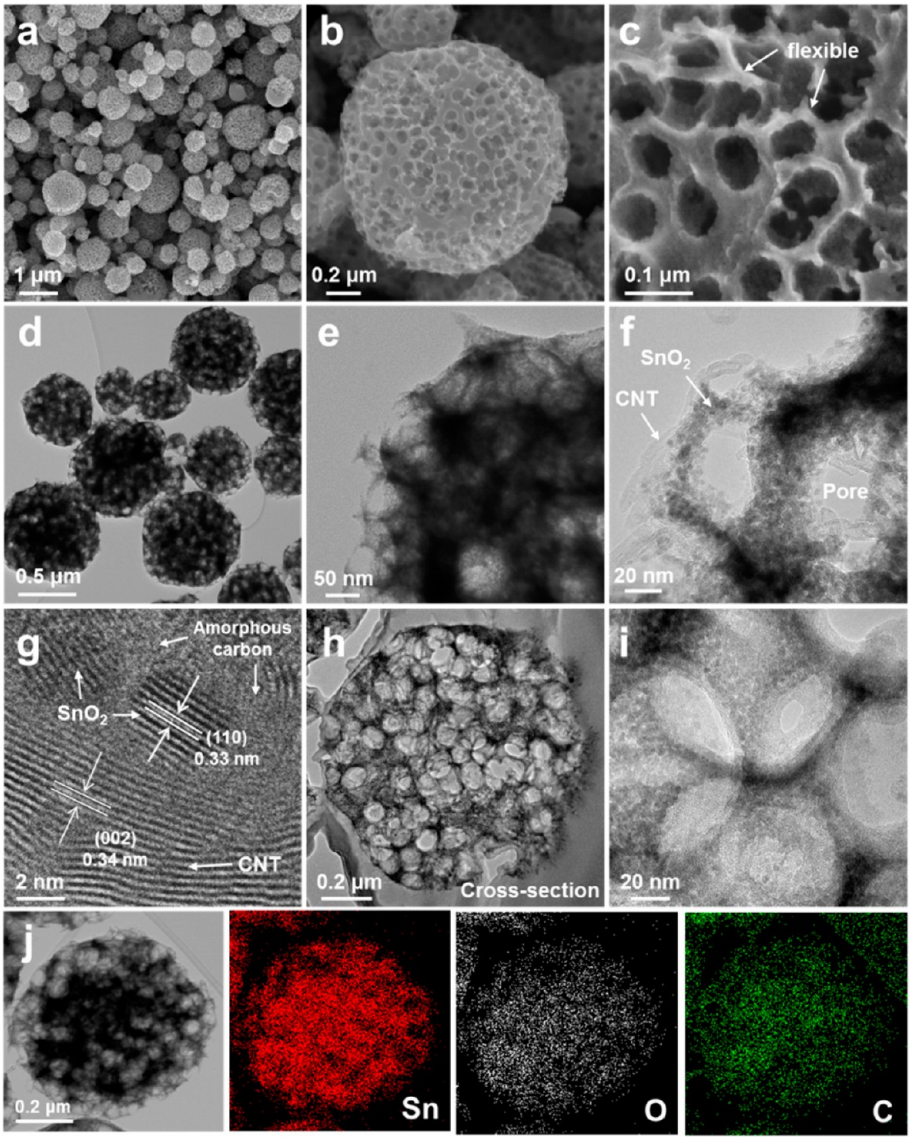

Figure 1. Morphologies and elemental mapping images of the perforated SnO_2–CNT composite microspheres. (a–c) FE-SEM images, (d,e) TEM images, (f,g) HR-TEM images, (h,i) cross section TEM images obtained by a FIB, and (j) elemental mapping images of tin, oxygen, and carbon components.

the microsphere. Scheme 1 shows the process of formation for bare metal oxide microspheres with a uniform distribution of void nanospheres and for filled metal oxide–CNT composite microspheres. Bare metal oxide microspheres with a uniform distribution of void nanospheres were prepared directly by spray pyrolysis from a spray solution containing PS nanobeads and metal salt as described in Scheme 1b. Metal oxide–CNT composite microspheres with a filled structure were prepared from a spray solution containing CNTs and metal salt as described in Scheme 1c.

Several types of metal oxide–CNT composite microspheres with a uniform distribution of void nanospheres were prepared by the one-step spray pyrolysis process. The morphologies of the tin oxide–CNT composite prepared from the spray solution with PS nanobeads and CNT fibers, which was studied as the main example, are shown in Figure 1. The composite microspheres had a uniformly spherical shape and did not aggregate, as shown in the low-resolution field-emission scanning electron microscopy (FE-SEM) image in Figure 1a. The size distribution of the perforated SnO_2–CNT composite microspheres measured from FE-SEM images is shown in Figure S2. The composite microspheres had an average size of 0.6 μm. The size of each composite microsphere was dependent on the size of the droplet from which it formed because one microsphere was formed by drying and decomposing one droplet. Therefore, the SnO_2–CNT composite microspheres prepared from the droplets formed by an ultrasonic nebulizer had broad size distribution, as shown in Figure S2. The SnO_2–CNT composite microspheres whose sizes were uniformly distributed could be prepared using spray pyrolysis with a well-established

atomizer or by introducing a droplet classifier between the droplet generator and the tubular furnace reactor to increase the sharpness of the size distribution of the prepared microspheres. The high-resolution FE-SEM images shown in Figure 1b,c show 70 nm macropores on the composite surface. A stretchable SnO_2−CNT composite structure surrounding the macropores appeared. Transmission electron microscopy (TEM) images in Figure 1d,e clearly show the porous structure of the composite microspheres. High-resolution (HR) TEM images in Figure 1f,g show 5 nm SnO_2 nanoparticles grafted uniformly on CNT backbones. The HR-TEM image (Figure 1g) exhibits clear lattice fringes separated by 0.33 and 0.34 nm, which correspond to the (110) crystal plane of the tetragonal SnO_2 phase and the (002) plane of the CNT layers, respectively.[45,46] The selected area electron diffraction (SAED) pattern of the SnO_2−CNT composite microspheres shows polycrystalline SnO_2 nanoparticles (Figure S3). To identify the inner structure of the composite microspheres, TEM images of the sample were obtained by a focus ion beam (FIB) instrument, as shown in Figure 1h,i. Figure 1h shows uniform void nanospheres dispersed within the composite microsphere. The HR-TEM image (Figure 1i) shows a uniform distribution of SnO_2 nanoparticles on a perforated structure. The elemental mapping images shown in Figure 1j show that the tin, oxygen, and carbon components are uniformly distributed over the entire composite microsphere. The uniform morphologies and uniform distributions of all components of the composite demonstrate the homogeneity of the SnO_2−CNT composite microspheres with a uniform distribution of void nanospheres prepared by one-step spray pyrolysis. The morphologies of perforated CNT microspheres prepared by the same process using a spray solution with PS nanobeads and oxidized CNTs are shown in Figure S4. FE-SEM and TEM images showed spherical CNT microspheres with macropores. The high-resolution TEM images shown in Figure S4e,f show cotton-ball-like CNTs with macropores. The morphologies of the bare SnO_2 and SnO_2−CNT composite microspheres prepared by one-step spray pyrolysis are shown in Figure 2. Bare SnO_2 microspheres prepared from the spray solution with PS nanobeads are spherical in shape with a perforated structure according to FE-SEM and TEM images in Figure 2a−e. The ultrafine SnO_2 nanospheres were connected to form a macroporous network, as shown in Figure 2f. The SnO_2−CNT composite microspheres prepared from the spray solution without PS nanobeads were spherical with a filled structure, as shown by the FE-SEM and TEM images in Figure 2g−l.

The X-ray diffraction (XRD) patterns of the three types of tin oxide samples can be indexed to tetragonal SnO_2 phase (JCPDS Card No. 41-1445) without impurity phases,[59] as shown in Figure 3a. According to Scherrer's formula, the average crystallite sizes of bare SnO_2, filled SnO_2−CNT composite, and perforated SnO_2−CNT composite microspheres were 5.4, 4.7, and 4.0 nm, respectively, which are consistent with TEM observations. X-ray photoelectron spectroscopy (XPS) measurements were carried out to study the chemical state of the elements in the perforated SnO_2−CNT composite microspheres. Similar to previous reports, the C 1s peak of the oxidized CNT fibers could be fitted to line shapes with binding energies at 284.6, 285.0, 286.3, 289.3, and 291.4 eV, which are assigned to C═C (sp^2), C−C (sp^3), C−O, C═O, and O−C═O, respectively.[60,61] The perforated SnO_2−CNT composite microspheres had C 1s XPS peaks of oxidized CNT fibers, as shown in Figure 3b. The XPS results proved that the surface of the MWCNTs is grafted with oxygen-containing groups after acid treatment. Figure S5 presents the Sn 3d peaks of the perforated SnO_2−CNT composite microspheres. The binding energies of Sn $3d_{5/2}$ and $3d_{3/2}$ were 495.9 and 487.4 eV, respectively, which correspond to the pure SnO_2 nanoparticles.[61] Figure S6 presents the XPS O 1s spectrum of the perforated SnO_2−CNT composite microspheres. The XPS O 1s spectrum of the perforated SnO_2−CNT composite microspheres showed a broad peak at 531.5 eV, which may be attributed to the SnO_2 nanoparticle and functional groups on the CNT surface.[60−62] Thus, tin oxalate was completely converted into the tetragonal SnO_2 phase inside the reactor that was maintained at 700 °C. Oxygen-deficient SnO and metallic Sn phases were not formed. The thermal gravimetric (TG) curve of the SnO_2−CNT composite microspheres with void nanospheres showed two-step weight loss below 600 °C, as shown in Figure 3c. The first slight weight loss observed at around 300 °C was due to the combustion of carbonaceous material remaining after the incomplete decomposition of PS nanobeads.[62] The second weight loss observed at around 450 °C was attributed to the combustion of CNTs. The weight losses in the SnO_2−CNT composite microspheres prepared at a preparation temperature of 700 °C by combustion of amorphous carbons and CNTs were 4 and 9 wt %, respectively. The weight losses in the SnO_2−CNT composite microspheres with perforated and filled structures due to the combustion of CNTs were both 9 wt %. To identify the amorphous carbon formed from incomplete decomposition of PS nanobeads, the XPS C 1s spectrum of the bare SnO_2 microspheres is shown in Figure S7. The binding energy of 284.6 eV for the XPS C 1s spectrum corresponds to the carbon atoms of amorphous carbon.[63] The Brunauer−Emmett−Teller (BET) surface areas of the bare SnO_2 and SnO_2−CNT composite microspheres with perforated and filled structures were 19.6, 83.1, and 53.7 $m^2\ g^{-1}$, respectively. The filled SnO_2−CNT composite microspheres had mesopores without macropores, as shown in Figure 3d. However, the bare SnO_2 and perforated

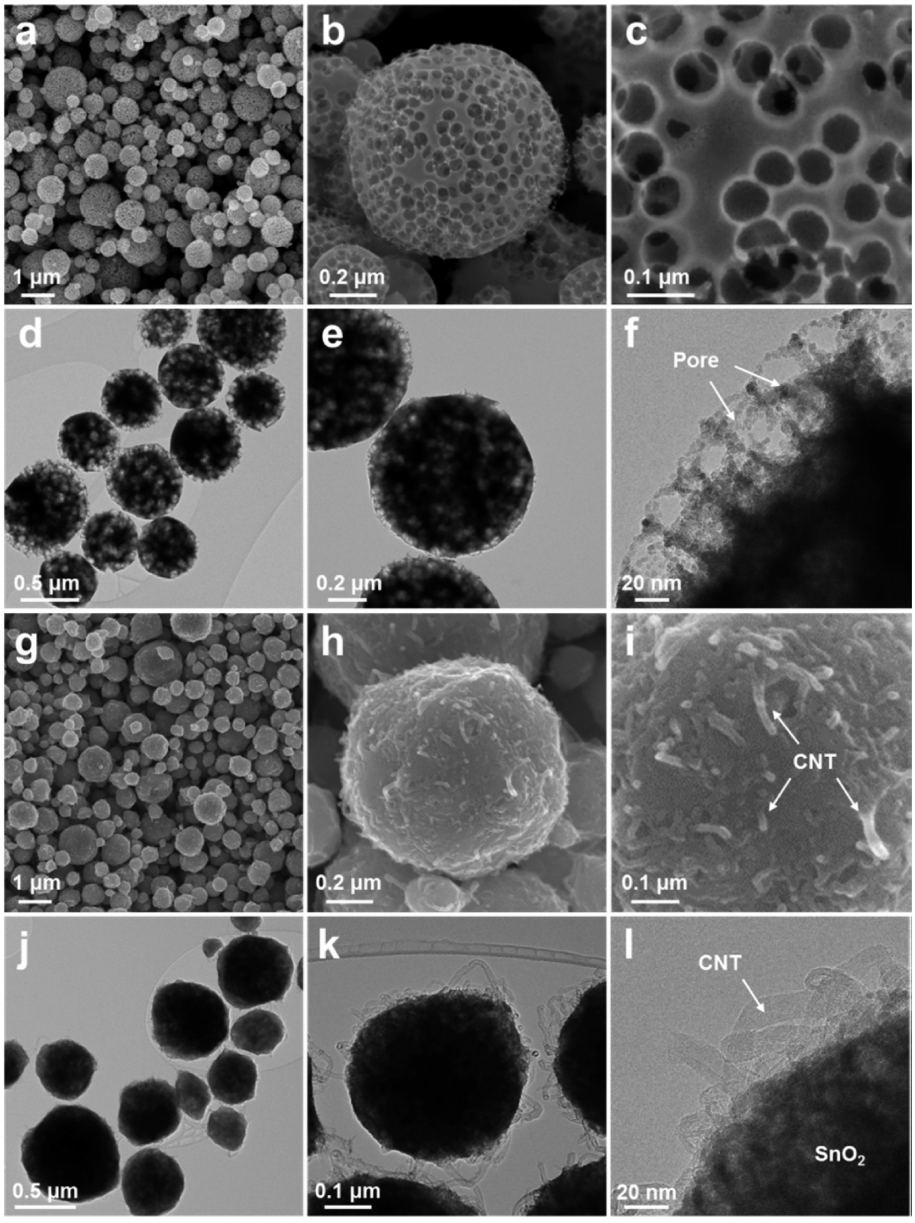

Figure 2. Morphologies of the bare SnO_2 and filled SnO_2–CNT composite microspheres. (a–c) FE-SEM and (d–f) TEM images of the bare SnO_2 microspheres with a uniform distribution of void nanospheres, and (g–i) FE-SEM and (j–l) TEM images of the filled SnO_2–CNT composite microspheres.

SnO_2–CNT composite microspheres had well-defined macropores due to the thermal decomposition of the PS nanobeads.[64]

The electrochemical properties of the three types of tin oxide microspheres were investigated by cyclic voltammetry (CV) and galvanostatic charge/discharge measurements to determine the effect of the void nanospheres and CNTs on the Li-ion storage properties of SnO_2. Figure 4a shows the CV curves of the tin oxide–CNT composite microspheres with a uniform distribution of void nanospheres from the first cycle to the fifth cycle at a scan rate of 0.1 mV s^{-1} in a potential range from 0.001 to 3.0 V. In the first cathodic sweep, the peak at 0.8 V can be ascribed to the electrochemical conversion of SnO_2 to Sn metal and Li_2O matrix and the formation of the solid electrolyte interphase (SEI) layer.[45–48,65–67] The peak below 0.5 V corresponds to the alloying reaction between 1 mol of Sn and 4.4 mol of Li. In the first anodic sweep, the peak centered at 0.5 V corresponds to the dealloying reaction of $Li_{4.4}Sn$ alloys.[45–48,65–67] Other broad peaks with weak intensities at 1.4 and 1.9 V may be related to the continuous dealloying of the Li_xSn phase and the conversion reaction of Sn into the SnO_x phase.[45–48,65–67] After the first cycle, all the CV curves are almost identical, which demonstrates that charge/discharge processes in the composite microspheres are highly reversible. Galvanostatic charge/discharge measurements were performed at a current density of 1.5 A g^{-1} in a potential window of 0.001–3.0 V *vs* Li^+/Li. The represented

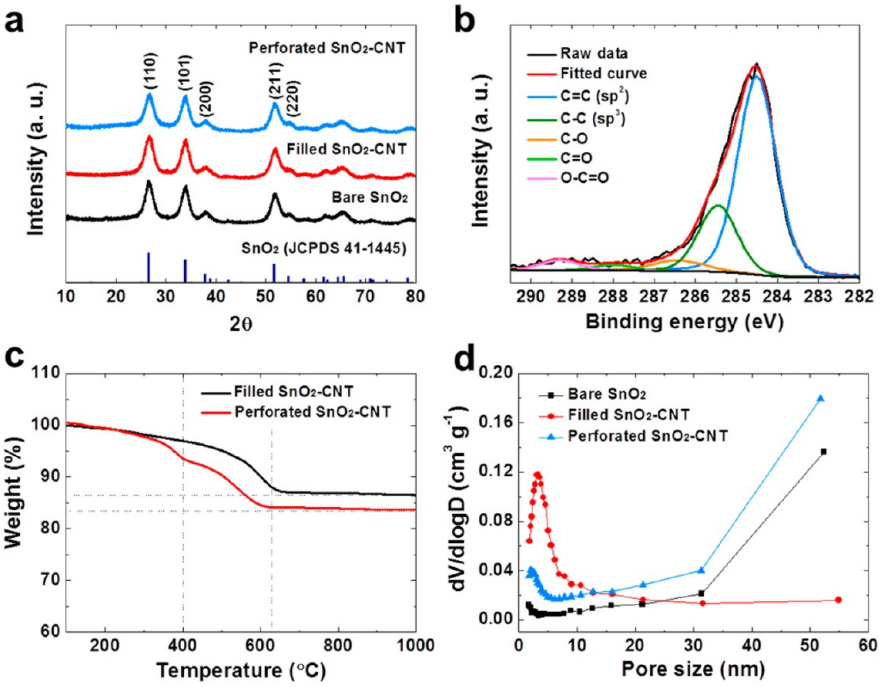

Figure 3. Characteristics of the bare SnO_2 and SnO_2–CNT composite microspheres with perforated and filled structures. (a) XRD patterns, (b) C 1s XPS spectrum of the perforated SnO_2–CNT composite microspheres, (c) TG curves, and (d) pore distributions.

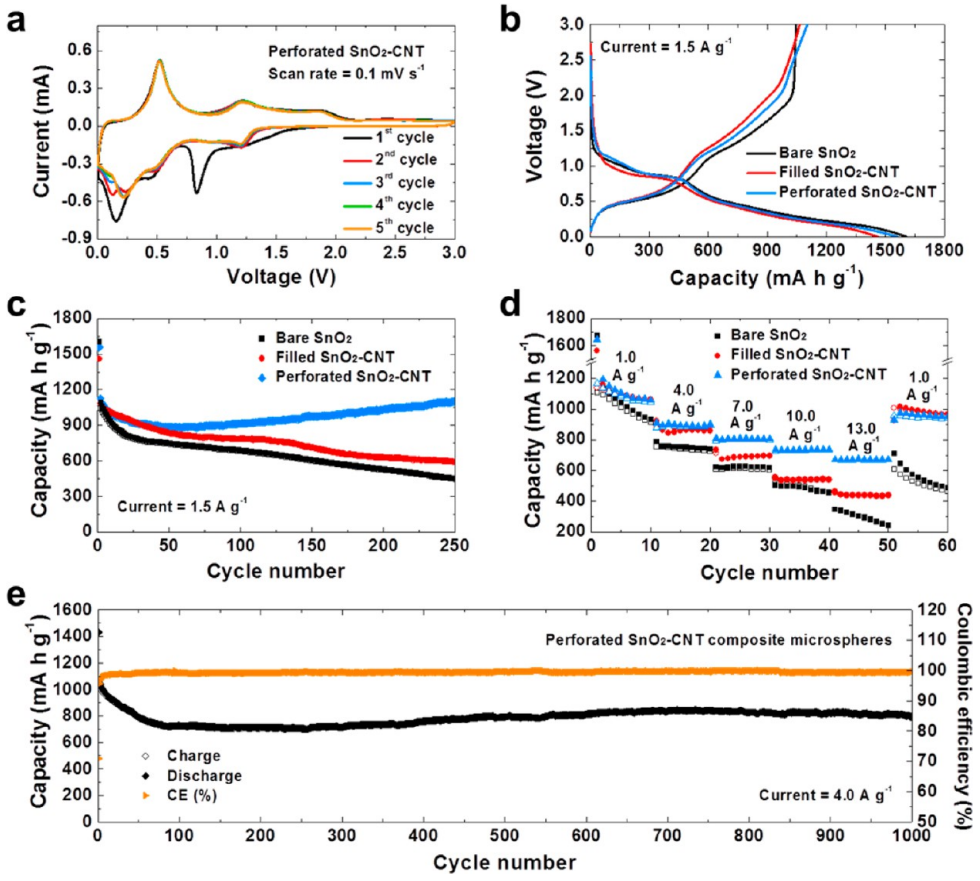

Figure 4. Characteristics of the bare SnO_2 and SnO_2–CNT composite microspheres with perforated and filled structures. (a) CV curves of the perforated SnO_2–CNT composite microspheres, (b) first cycle profiles of all samples at a current density of 1.5 A g^{-1}, (c) cycling performances at a current density of 1.5 A g^{-1}, (d) rate performances of all samples at various current densities, and (e) long-term cycling performance of the perforated SnO_2–CNT composite microspheres.

specific capacity was calculated based on the total mass of the SnO_2–CNT composite. Figure 4b shows the initial discharge and charge curves of the three samples. The three samples had similar discharge and charge profiles regardless of the CNT additive. The initial discharge capacities of the bare SnO_2 and SnO_2–CNT composite microspheres with perforated and filled structures were 1604, 1559, and 1459 mA h g^{-1}, respectively, and their corresponding initial Coulombic efficiencies were 65, 71, and 73%. The initial irreversible capacities of all samples could be caused by the formation of a SEI layer, as indicated in the CV curve of the first cycle and the partial structural damage during the first cycle. The initial discharge and charge capacities of the perforated CNTs, at a current density of 1.5 A g^{-1}, were 1200 and 400 mA h g^{-1}, respectively (Figure S8a), and its corresponding initial Coulombic efficiency was 33%. The low initial Coulombic efficiency was mainly attributed to the electrolyte decomposition and SEI formation on the perforated CNT surfaces.[45−47] After 100 cycles, the perforated CNT microspheres delivered a discharge capacity of 305 mA h g^{-1} at a high current density of 1.5 A g^{-1}. Detailed cycle profiles of the perforated CNT microspheres are shown in Figure S8b. The cycling performances of the three samples at a constant current density of 1.5 A g^{-1} are shown in Figure 4c. Detailed cycle profiles of all samples are given in Figure S9. The discharge capacities of the bare SnO_2 and SnO_2–CNT composite microspheres with a filled structure decreased continuously over 250 cycles. The discharge capacities of the perforated SnO_2–CNT composite microspheres also decreased over the first 20 cycles. The capacity fading during cycling was due to the transformation of the crystalline structure to a stable, amorphous structure, the mechanical degradation of metal oxide, and the formation of an unstable SEI layer during cycling.[68,69] The bare SnO_2 and SnO_2–CNT composite microspheres with perforated and filled structures delivered discharge capacities of 450, 1108, and 590 mA h g^{-1} for the 250th cycle, and the corresponding capacity retentions measured from the second cycle were 41, 98, and 55%, respectively. To understand the excellent reversible capacities of the perforated SnO_2–CNT composite microspheres, the morphologies of the perforated SnO_2–CNT composite microspheres obtained after 1, 50, 150, and 250 cycles were investigated by SEM and TEM images, as shown in Figures S10–S13. The overall morphologies of the SnO_2–CNT microspheres were maintained even after 250 cycles. However, the TEM and elemental mapping images of the microspheres revealed the transformation of the metallic Sn nanocrystals formed during the first cycle into amorphous-like material. The high mechanical degradation of the bare SnO_2 and SnO_2–CNT composite microspheres with filled structure decreased continuously with the discharge capacities during cycling. However, the reversible capacities of the perforated SnO_2–CNT composite microspheres increased gradually during the subsequent 230 cycles. This phenomenon was due to the formation of a polymeric, gel-like film on the perforated SnO_2–CNT composite microspheres.[70]

The rate capabilities of the bare SnO_2 and SnO_2–CNT composite microspheres with perforated and filled structures were evaluated by applying high current densities from 1.0 to 13.0 A g^{-1} (Figure 4d). Ten cycles were measured during each increment to evaluate the rate performance. The perforated SnO_2–CNT composite microspheres exhibited high 10th cycle reversible capacities of 1060, 901, 806, 738, and 671 mA h g^{-1} at current densities of 1.0, 4.0, 7.0, 10.0, and 13.0 A g^{-1}, respectively. However, the filled SnO_2–CNT composite microspheres exhibited high 10th cycle reversible capacities of 1062, 862, 698, 539, and 437 mA h g^{-1} at current densities of 1.0, 4.0, 7.0, 10.0, and 13.0 A g^{-1}, respectively. The bare SnO_2 exhibited high 10th cycle reversible capacities of 932, 738, 620, 453, and 246 mA h g^{-1} at current densities of 1.0, 4.0, 7.0, 10.0, and 13.0 A g^{-1}, respectively. Detailed cycle profiles of the all samples used to determine the rate performances are given in Figure S14. The rate retentions of the bare SnO_2 and SnO_2–CNT composite microspheres with perforated and filled structures were 26, 63, and 41%, respectively, when the current density increased from 1.0 to 13.0 A g^{-1}. The reversible discharge capacities of the SnO_2–CNT composite microspheres with perforated and filled structures recovered well when the current density was restored to 1 A g^{-1}. However, the discharge capacities of the bare SnO_2 microspheres did not recover when the current density was restored to 1 A g^{-1}. The long-term cycling performance of the perforated SnO_2–CNT composite microspheres at a high current density of 4 A g^{-1} is shown in Figure 4e. The initial discharge and charge capacities of the composite microspheres were 1432 and 1016 mA h g^{-1}, respectively. In the initial cycling range of 2–100 cycles, the reversible discharge capacities deceased from 1068 to 729 mA h g^{-1}. After the 100th cycle, the perforated SnO_2–CNT composite microspheres showed stable Li-ion storage properties. The reversible capacity and Coulombic efficiency of the 1000th cycle were 796 mA h g^{-1} and 99.6%, respectively. The electrochemical properties of the perforated SnO_2–CNT composite microspheres prepared by one-step spray pyrolysis are compared to those of SnO_2–CNT composite powders with various morphologies reported previously in the literature, and the results are summarized in Table 1. The perforated SnO_2–CNT composite microspheres obtained in the present study seem to show markedly superior cycling and rate performances compared to values previously reported for various SnO_2–CNT composites. The perforated structure of the SnO_2–CNT composite microspheres with a uniform distribution

TABLE 1. Comparison of the Li-Ion Storage Properties of Perforated SnO_2–CNT Composite Microspheres to Those of Reported SnO_2–CNT Composite Materials

typical examples	voltage range (V)	current density (mA g^{-1})	cycle number	reversible capacity (mA h g^{-1})	ref
cross-stacked CNT loaded with SnO_2	0.01–3.0	88	65	850	44
SnO_2-coated CNT	0.05–2.0	100	100	473	45
core–shell SnO_2@CNT	0.01–2.5	0.2 (mA cm^{-2})	50	627	46
SnO_2–CNT composite	0.001–2.5	500	250	420	47
SnO_2@MWCNT@SnO_2@PPy coaxial nanocables	0.01–2.5	100	30	600	48
SnO_2–CNT composite	0.01–1.5	0.1 (mA cm^{-2})	50	473	49
nano-SnO_2 in CNTs	0.01–1.5	100	300	370	50
SnO_2 nanoparticles on CNT	0.5–3.0	800	100	754	51
SnO_2–CNT nanocomposites	0.005–2.0	200	30	400	52
CNT anchored with SnO_2 nanosheets	0–3.0	100	40	579	53
perforated SnO_2–CNT composite microspheres	0.001–3.0	1500	250	1108	this work
		10000	1000	796	

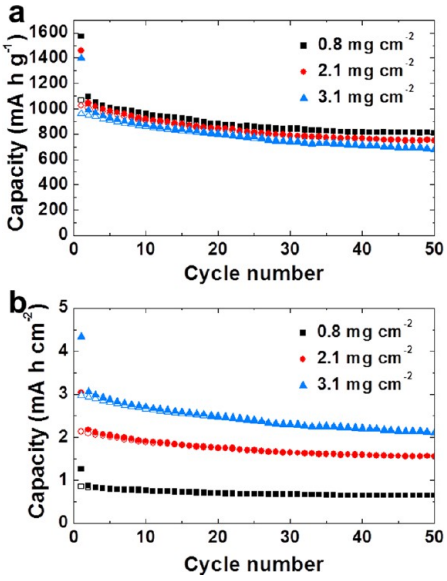

Figure 5. (a) Gravimetric and (b) areal capacities of the perforated SnO_2–CNT composite microspheres at the different SnO_2 mass loadings on the electrode.

of void nanospheres not only enabled electrolyte penetration within composite microspheres to decrease the Li-ion diffusion path but also provided void space for the volume expansion during charge/discharge cycles. In addition, the CNT-based flexible backbone of the composite microspheres improved the electrical conductivity within the microsphere and improved the structural stability during cycling.

The areal and volumetric capacity is an important factor for practical electrode materials.[71] The gravimetric and areal capacities of the perforated SnO_2–CNT composite microspheres at the SnO_2 mass loadings of 0.8, 2.1, and 3.1 mg cm^{-2} are shown in Figure 5. The electrode was prepared from a mixture containing 80 wt % of the active material, 10 wt % of Super P, and 10 wt % of sodium carboxymethyl cellulose binder. The current density of all electrodes was fixed at 1 A g^{-1}. The initial gravimetric discharge capacities of the perforated SnO_2–CNT composite microspheres at the loading amounts of 0.8, 2.1, and 3.1 mg cm^{-2} were 1570, 1459, and 1401 mA h g^{-1}, respectively, and their initial gravimetric charge capacities were 1067, 1025, and 963 mA h g^{-1}, respectively. After 50 cycles, the perforated SnO_2–CNT composite microspheres at the loading amounts of 0.8, 2.1, and 3.1 mg cm^{-2} delivered the gravimetric discharge capacities of 807, 752, and 681 mA h g^{-1}, respectively. The initial areal discharge capacities of the perforated SnO_2–CNT composite microspheres at the loading amounts of 0.8, 2.1, and 3.1 mg cm^{-2} were 1.25, 3.03, and 4.33 mA h cm^{-2}, respectively, and their initial areal charge capacities were 0.85, 2.13, and 2.98 mA h cm^{-2}. After 50 cycles, the perforated SnO_2–CNT composite microspheres at the loading amounts of 0.8, 2.1, and 3.1 mg cm^{-2} delivered areal discharge capacities of 0.65, 1.56, and 2.11 mA h cm^{-2}, respectively. In this study, the thickness of the perforated SnO_2–CNT electrodes at a 2.1 mg cm^{-2} of mass loading was about 17 μm, as shown in Figure S15. Furthermore, the initial volumetric discharge and charge capacities of the perforated SnO_2–CNT composite microspheres at the loading amount of 2.1 mg cm^{-2} were high as 1782 and 1253 mA h cm^{-3}, respectively. The 50th volumetric discharge capacity at a high current density of 2.1 mA cm^{-2} was 917 mA h cm^{-3}, and its volumetric capacity was higher than 400–500 mA h cm^{-3} of the commercial graphite electrode.[72,73] Figure S16 shows the TEM images of the perforated SnO_2–CNT composite microspheres prepared from the spray solution with small-sized PS nanobeads (30 nm). The TEM images revealed that the composite microspheres possessed more filled structure than the sample prepared from the spray solution with large-sized PS nanobeads. The elemental mapping images shown in Figure S16 revealed the uniform distribution of Sn and C components in the entirety of the perforated SnO_2–CNT composite microspheres. The perforated SnO_2–CNT composite microspheres prepared by spray pyrolysis exhibited high initial gravimetric

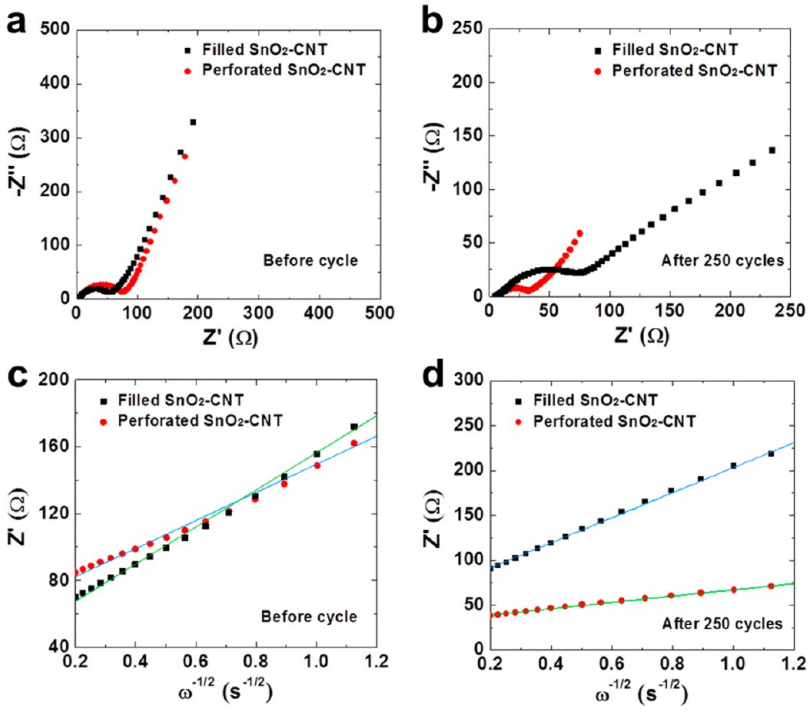

Figure 6. Electrochemical impedance spectroscopy (EIS) and relationship between Z' and $\omega^{-1/2}$ in the low-frequency region of SnO_2–CNT composite microspheres with perforated and filled structures. (a,b) EIS spectra before cycling and after 250th cycle. (c,d) Linear fits in the low-frequency region before cycling and after the 250th cycle.

capacities and good cycling performance, as shown in Figure S17.

To investigate the effect of void nanospheres on the structural stability of SnO_2–CNT composite microspheres, impedance measurements were carried out before cycling and after 250 cycles at a constant current density of 1.5 A g^{-1}, as shown Figure 6. The medium-frequency semicircle is attributed to the charge-transfer resistance (R_{ct}) between the active material and the electrolyte.[74−78] The low-frequency region corresponds to Li-ion diffusion within the active materials. The charge-transfer resistance of the electrode materials before cycling was critically affected by the BET surface area, crystallinity, and contact area with the liquid electrolyte.[74,75] Before cycling, the charge-transfer resistances of SnO_2–CNT composite microspheres with perforated and filled structures were 78 and 58 Ω, respectively. The perforated SnO_2–CNT composite microspheres had a large contact area with electrolyte, and thus their charge-transfer resistance was larger than that of the filled microspheres. However, the charge-transfer resistances of the microspheres with perforated and filled structures were 32 and 88 Ω after the 250th cycle, respectively, as shown in Figure 6b. The relationship between Z_{re} and $\omega^{-1/2}$ in the low-frequency region, where ω is the angular frequency in the low-frequency region ($\omega = 2\pi f$), is shown in Figure 6c,d.[58,76−78] The low slope of the fitted curve at low frequency indicates good Li-ion kinetics in the electrode materials. The perforated SnO_2–CNT composite microspheres led to a slope lower than that of the filled composite microspheres before and after cycling. Especially, the perforated SnO_2–CNT composite microspheres showed good Li-ion kinetics after 250 cycles. The low charge-transfer resistance and excellent Li-ion diffusion properties of the perforated SnO_2–CNT composite microspheres during long-term cycling were due to synergetic combination of highly conductive CNTs and the morphological advantage of void nanospheres.

Furthermore, the strategy described in this study has generally applied to various metal oxide–CNT composites with perforated structures. We successfully synthesized many other metal oxide–CNT composites, such as NiO, WO_3, and GeO_2. Figure 7 shows typical SEM and TEM images of NiO–CNT (Figure 7a–d), WO_3–CNT (Figure 7e–h), and GeO_2–CNT (Figure 7i–l) composite microspheres with perforated structures. Similar perforated structures formed in these three samples, which were synthesized using continuous, one-step, and high-yield spray pyrolysis with a spraying solution of metal salts, PS nanobeads, and oxidized CNTs. There were some slight differences in surface roughness between the structures due to the unique physical characteristics of each material. TEM images of the perforated NiO–CNT composite showed that the NiO nanoparticles were spherical, as shown in Figure 7c,d. However, TEM images of perforated WO_3–CNT and GeO_2–CNT composites showed nanorod and amorphous structures, respectively. Differences in morphology could originate from the different crystallization and crystal growth behavior of metal oxides

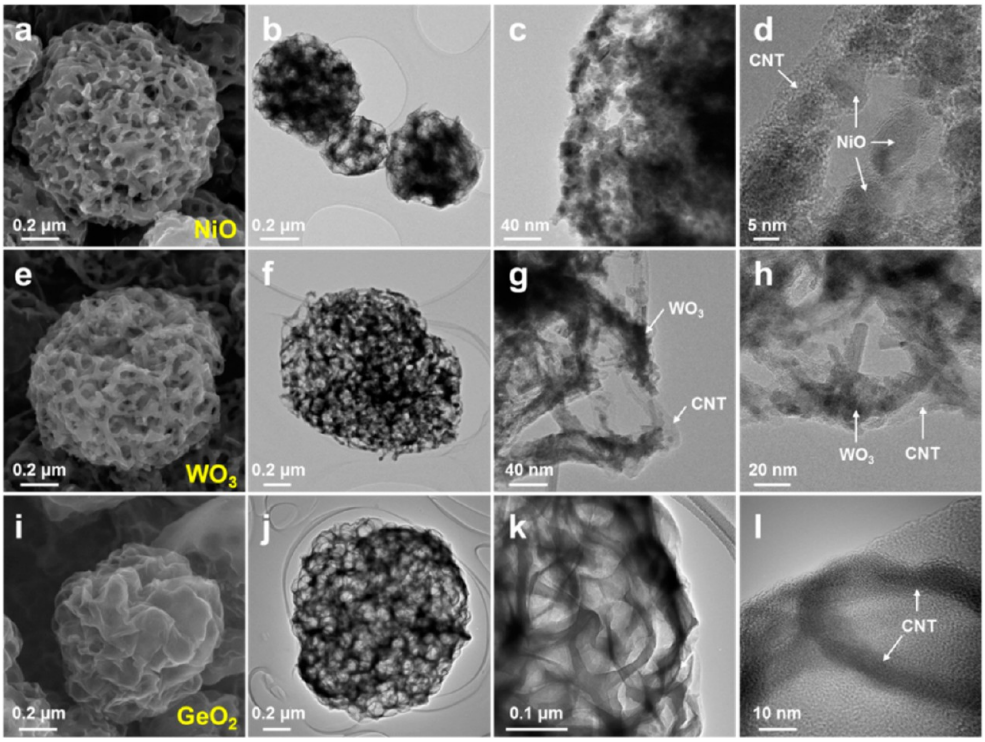

Figure 7. Morphologies of perforated metal oxide−CNT composite microspheres. (a) FE-SEM and (b−d) TEM images of the NiO−CNT composite; (e) FE-SEM and (f−h) TEM images of the WO_3−CNT composite; and (i) FE-SEM and (j−l) TEM images of the GeO_2−CNT composite.

in a hot-wall reactor maintained at 700 °C. In addition, low-resolution FE-SEM images and elemental mapping images of the three samples shown in Figures S18−S20 showed that one-step synthesis produced overall uniform composite microspheres. The contents of carbonaceous materials in the perforated NiO−CNT, WO_3−CNT, and GeO_2−CNT composite microspheres measured by energy-dispersive spectroscopy analysis were 20, 20, and 23%, as shown in Figure S21. Therefore, this effective and innovative strategy could be applied to the preparation of perforated metal oxide−CNT composites with complex elemental compositions using water-soluble metal salts, PS nanobeads, and oxidized CNTs for many applications.

CONCLUSIONS

Perforated metal oxide−CNT composite microspheres with a uniform distribution of void nanospheres were prepared by a simple, one-pot, spray pyrolysis process. PS nanobeads added as an organic template formed void nanospheres within the metal oxide−CNT composite microsphere. The synergetic combination of highly conductive CNTs and the morphological advantage of void nanospheres resulted in the excellent lithium-ion storage properties of SnO_2−CNT composite microspheres, which were selected as the first target material. The void volume and CNT content of the metal oxide−CNT composite microspheres could be easily controlled by changing the amounts of PS nanobeads and oxidized CNTs in the spray solution. The type of metal oxide could be also varied from single to multicomponent by changing the water-soluble metal salts. Therefore, the simple, one-step process developed in this study can be applied to the preparation of perforated metal oxide−CNT composite microspheres with various compositions and controlled morphologies for widespread applications, including energy storage.

EXPERIMENTAL DETAILS

Synthesis Method. Oxidized multiwalled CNTs (MWCNTs) were modified using a HNO_3/H_2SO_4 (1:3 vol %) solution at 70 °C.[53] The acid-treated MWCNTs were washed using distilled water and ethanol solution five times and redispersed in distilled water. Metal salts were added to 500 mL of 100 nm PS nanobeads (3.0 g) and acid-treated MWCNTs (1 mg mL^{-1}) to prepare the perforated metal oxide−CNT composite microspheres through the one-step spray pyrolysis at 700 °C. The metal salts were tin oxalate (Aldrich), nickel nitrate hexahydrate (Junsei), ammonium metatungstate (Aldrich), and germanium oxide (Samchun). A quartz reactor, 1200 mm in length and 50 mm in diameter, was used with an Ar gas flow rate (carrier gas) of 10 L min^{-1}. A colloidal spray solution containing CNTs, without PS nanobeads, was used to prepare filled metal oxide−CNT composite microspheres directly.

Characterizations. The crystal structures of the samples prepared through the one-step spray pyrolysis process were investigated using X-ray diffractometry (X'pert PRO MPD) with

Cu Kα radiation (λ = 1.5418 Å). The morphological features were investigated using FE-SEM (Hitachi S-4800) and high-resolution transmission electron microscopy (JEM-2100F) at a working voltage of 200 kV. The specific surface areas of the microspheres were calculated from a BET analysis of nitrogen adsorption measurements (TriStar 3000). The microspheres were also investigated using XPS (ESCALAB-210) with Al Kα radiation (1486.6 eV). A thermal gravimetric analysis (TGA; SDT Q600) was performed in air at a heating rate of 20 °C min^{-1} to determine the amount of CNTs in the composite microspheres.

Electrochemical Measurements. The capacities and cycling properties of the samples were determined using a 2032-type coin cell battery. The electrode was prepared from a mixture containing 70 wt % of the active material, 20 wt % of Super P, and 10 wt % of sodium carboxymethyl cellulose binder. Li metal and microporous polypropylene film were used as the counter electrode and separator, respectively. The electrolyte was a solution of 1 M $LiPF_6$ in a 1:1 volume mixture of ethylene carbonate/dimethyl carbonate to which 5 wt % fluoroethylene carbonate was added. The charge−discharge characteristics of the samples were determined by cycling in a potential range of 0.001−3.0 V at fixed current densities. CV was carried out at a scan rate of 0.1 mV s^{-1}. The dimensions of the negative electrode were 1 cm × 1 cm, and the active mass loading of the active materials was approximately 1.0 mg cm^{-2}. Electrochemical impedance analysis was performed using electrochemical impedance spectroscopy over a frequency range of 100 kHz to 0.01 Hz.

Conflict of Interest: The authors declare no competing financial interest.

Supporting Information Available: The Supporting Information is available free of charge on the ACS Publications website at DOI: 10.1021/acsnano.5b03822.

Additional information (PDF)

Acknowledgment. This work is supported by the National Research Foundation of Korea (NRF) grant funded by the Korea Government (MEST) (No. 2013R1A2A1A01006545).

REFERENCES AND NOTES

1. Aricò, A. S.; Bruce, P.; Scrosati, B.; Tarascon, J.-M.; van Schalkwijk, W. Nanostructured Materials for Advanced Energy Conversion and Storage Devices. *Nat. Mater.* **2005**, *4*, 366–377.
2. Wang, Z.; Zhou, L.; Lou, X. W. Metal Oxide Hollow Nanostructures for Lithium-Ion Batteries. *Adv. Mater.* **2012**, *24*, 1903–1911.
3. Cheng, F.; Liang, J.; Tao, Z.; Chen, J. Functional Materials for Rechargeable Batteries. *Adv. Mater.* **2011**, *23*, 1695–1715.
4. Lai, X.; Halpert, J. E.; Wang, D. Recent Advances in Micro-/Nano-Structured Hollow Spheres for Energy Applications: From Simple to Complex Systems. *Energy Environ. Sci.* **2012**, *5*, 5604–5618.
5. Gogotsi, Y. What Nano Can Do for Energy Storage. *ACS Nano* **2014**, *8*, 5369–5371.
6. Choi, N.-S.; Chen, Z.; Freunberger, S. A.; Ji, X.; Sun, Y.-K.; Amine, K.; Yushin, G.; Nazar, L. F.; Cho, J.; Bruce, P. G. Challenges Facing Lithium Batteries and Electrical Double-Layer Capacitors. *Angew. Chem., Int. Ed.* **2012**, *51*, 9994–10024.
7. Song, M.-K.; Park, S.; Alamgir, F. M.; Cho, J.; Liu, M. Nanostructured Electrodes for Lithium-Ion and Lithium-Air Batteries: the Latest Developments, Challenges, and Perspectives. *Mater. Sci. Eng., R* **2011**, *72*, 203–252.
8. Zhao, M.-Q.; Ren, C. E.; Ling, Z.; Lukatskaya, M. R.; Zhang, C.; Van Aken, K. L.; Barsoum, M. W.; Gogotsi, Y. Flexible MXene/Carbon Nanotube Composite Paper with High Volumetric Capacitance. *Adv. Mater.* **2015**, *27*, 339–345.
9. Jiang, J.; Li, Y.; Liu, J.; Huang, X.; Yuan, C.; Lou, X. W. Recent Advances in Metal Oxide-Based Electrode Architecture Design for Electrochemical Energy Storage. *Adv. Mater.* **2012**, *24*, 5166–5180.
10. Li, X.; Gu, M.; Hu, S.; Kennard, R.; Yan, P.; Chen, X.; Wang, C.; Sailor, M. J.; Zhang, J.-G.; Liu, J. Mesoporous Silicon Sponge as an Anti-Pulverization Structure for High-Performance Lithium-Ion Battery Anodes. *Nat. Commun.* **2014**, *5*, 4105.
11. Mai, L.; Tian, X.; Xu, X.; Chang, L.; Xu, L. Nanowire Electrodes for Electrochemical Energy Storage Devices. *Chem. Rev.* **2014**, *114*, 11828–11862.
12. Uchaker, E.; Cao, G. Mesocrystals as Electrode Materials for Lithium-Ion Batteries. *Nano Today* **2014**, *9*, 499–524.
13. Vu, A.; Qian, Y.; Stein, A. Porous Electrode Materials for Lithium-Ion Batteries − How to Prepare Them and What Makes Them Special. *Adv. Energy Mater.* **2012**, *2*, 1056–1085.
14. Pikul, J. H.; Zhang, H. G.; Cho, J.; Braun, P. V.; King, W. P. High-Power Lithium Ion Microbatteries from Interdigitated Three-Dimensional Bicontinuous Nanoporous Electrodes. *Nat. Commun.* **2013**, *4*, 1732.
15. Stein, A.; Wilson, B. E.; Rudisill, S. G. Design and Functionality of Colloidal-Crystal-Templated Materials−Chemical Applications of Inverse Opals. *Chem. Soc. Rev.* **2013**, *42*, 2763–2803.
16. Lee, K. T.; Lytle, J. C.; Ergang, N. S.; Oh, S. M.; Stein, A. Synthesis and Rate Performance of Monolithic Macroporous Carbon Electrodes for Lithium-Ion Secondary Batteries. *Adv. Funct. Mater.* **2005**, *15*, 547–556.
17. Hao, G.-P.; Han, F.; Guo, D.-C.; Fan, R.-J.; Xiong, G.; Li, W.-C.; Lu, A.-H. Monolithic Carbons with Tailored Crystallinity and Porous Structure as Lithium-Ion Anodes for Fundamental Understanding Their Rate Performance and Cycle Stability. *J. Phys. Chem. C* **2012**, *116*, 10303–10311.
18. Zhang, H.; Yu, X.; Braun, P. V. Three-Dimensional Bicontinuous Ultrafast-Charge and -Discharge Bulk Battery Electrodes. *Nat. Nanotechnol.* **2011**, *6*, 277–281.
19. Ko, Y. N.; Park, S. B.; Choi, S. H.; Kang, Y. C. One-Pot Synthesis of Manganese Oxide-Carbon Composite Microspheres with Three Dimensional Channels for Li-Ion Batteries. *Sci. Rep.* **2014**, *4*, 5751.
20. Huang, X.; Chen, J.; Lu, Z.; Yu, H.; Yan, Q.; Hng, H. H. Carbon Inverse Opal Entrapped with Electrode Active Nanoparticles as High-Performance Anode for Lithium-Ion Batteries. *Sci. Rep.* **2013**, *3*, 2317.
21. Choi, S. H.; Ko, Y. N.; Jung, K. Y.; Kang, Y. C. Macroporous Fe_3O_4/Carbon Composite Microspheres with a Short Li^+ Diffusion Pathway for the Fast Charge/Discharge of Lithium Ion Batteries. *Chem. - Eur. J.* **2014**, *20*, 11078–11083.
22. Thakur, M.; Sinsabaugh, S. L.; Isaacson, M. J.; Wong, M. S.; Biswal, S. L. Inexpensive Method for Producing Macroporous Silicon Particulates (MPSPs) with Pyrolyzed Polyacrylonitrile for Lithium Ion Batteries. *Sci. Rep.* **2012**, *2*, 795.
23. Li, Y.; Li, J. Carbon-Coated Macroporous $Sn_2P_2O_7$ as Anode Materials for Li-Ion Battery. *J. Phys. Chem. C* **2008**, *112*, 14216–14219.
24. An, Q.; Lv, F.; Liu, Q.; Han, C.; Zhao, K.; Sheng, J.; Wei, Q.; Yan, M.; Mai, L. Amorphous Vanadium Oxide Matrixes Supporting Hierarchical Porous Fe_3O_4/Graphene Nanowires as a High-Rate Lithium Storage Anode. *Nano Lett.* **2014**, *14*, 6250–6256.
25. Huang, X.; Zeng, Z.; Fan, Z.; Liu, J.; Zhang, H. Graphene-Based Electrodes. *Adv. Mater.* **2012**, *24*, 5979–6004.
26. Wu, Z.-S.; Zhou, G.; Yin, L.-C.; Ren, W.; Li, F.; Cheng, H.-M. Graphene/Metal Oxide Composite Electrode Materials for Energy Storage. *Nano Energy* **2012**, *1*, 107–131.
27. Li, Q.; Mahmood, N.; Zhu, J.; Hou, Y.; Sun, S. Graphene and Its Composites with Nanoparticles for Electrochemical Energy Applications. *Nano Today* **2014**, *9*, 668–683.
28. Wang, H.; Feng, H.; Li, J. Graphene and Graphene-Like Layered Transition Metal Dichalcogenides in Energy Conversion and Storage. *Small* **2014**, *10*, 2165–2181.
29. Chen, J. S.; Lou, X. W. SnO_2-Based Nanomaterials: Synthesis and Application in Lithium-Ion Batteries. *Small* **2013**, *9*, 1877–1893.
30. Zhang, L.; Zhang, G.; Wu, H. B.; Yu, L.; Lou, X. W. Hierarchical Tubular Structures Constructed by Carbon-Coated SnO_2 Nanoplates for Highly Reversible Lithium Storage. *Adv. Mater.* **2013**, *25*, 2589–2593.
31. Sun, W.; Wang, Y. Graphene-Based Nanocomposite Anodes for Lithium-Ion Batteries. *Nanoscale* **2014**, *6*, 11528–11552.

32. Mao, S.; Lu, G.; Chen, J. Three-Dimensional Graphene-Based Composites for Energy Applications. *Nanoscale* **2015**, *7*, 6924–6943.
33. Liang, J.; Yu, X.-Y.; Zhou, H.; Wu, H. B.; Ding, S.; Lou, X. W. Bowl-like SnO_2@Carbon Hollow Particles as an Advanced Anode Material for Lithium-Ion Batteries. *Angew. Chem., Int. Ed.* **2014**, *53*, 12803–12807.
34. Xin, S.; Guo, Y.-G.; Wan, L.-J. Nanocarbon Networks for Advanced Rechargeable Lithium Batteries. *Acc. Chem. Res.* **2012**, *45*, 1759–1769.
35. Landi, B. J.; Ganter, M. J.; Cress, C. D.; DiLeo, R. A.; Raffaelle, R. P. Carbon Nanotubes for Lithium Ion Batteries. *Energy Environ. Sci.* **2009**, *2*, 638–654.
36. Zhang, Q.; Huang, J.-Q.; Qian, W.-Z.; Zhang, Y.-Y.; Wei, F. The Road for Nanomaterials Industry: a Review of Carbon Nanotube Production, Post-Treatment, and Bulk Applications for Composites and Energy Storage. *Small* **2013**, *9*, 1237–1265.
37. Du, R.; Zhao, Q.; Zhang, N.; Zhang, J. Macroscopic Carbon Nanotube-Based 3D Monoliths. *Small* **2015**, *11*, 3263–3289.
38. Jia, X.; Cheng, Y.; Lu, Y.; Wei, F. Building Robust Carbon Nanotube-Interweaved-Nanocrystal Architecture for High-Performance Anode Materials. *ACS Nano* **2014**, *8*, 9265–9273.
39. Zhao, X.; Johnston, C.; Grant, P. S. A Novel Hybrid Supercapacitor with a Carbon Nanotube Cathode and an Iron Oxide/Carbon Nanotube Composite Anode. *J. Mater. Chem.* **2009**, *19*, 8755–8760.
40. Xu, C.; Sun, J.; Gao, L. Large Scale Synthesis of Nickel Oxide/Multiwalled Carbon Nanotube Composites by Direct Thermal Decomposition and Their Lithium Storage Properties. *J. Power Sources* **2011**, *196*, 5138–5142.
41. Fang, Z.; Xu, W.; Huang, T.; Li, M.; Wang, W.; Liu, Y.; Mao, C.; Meng, F.; Wang, M.; Cheng, M.; et al. Facile Scalable Synthesis of Co_3O_4/Carbon Nanotube Hybrids as Superior Anode Materials for Lithium-Ion Batteries. *Mater. Res. Bull.* **2013**, *48*, 4419–4423.
42. Ban, C.; Wu, Z.; Gillaspie, D. T.; Chen, L.; Yan, Y.; Blackburn, J. L.; Dillon, A. C. Nanostructured Fe_3O_4/SWNT Electrode: Binder-Free and High-Rate Li-Ion Anode. *Adv. Mater.* **2010**, *22*, E145–E149.
43. Chen, X.; Zhu, H.; Chen, Y.-C.; Shang, Y.; Cao, A.; Hu, L.; Rubloff, G. W. MWCNT/V_2O_5 Core/Shell Sponge for High Areal Capacity and Power Density Li-Ion Cathodes. *ACS Nano* **2012**, *6*, 7948–7955.
44. Zhang, H.-X.; Feng, C.; Zhai, Y.-C.; Jiang, K.-L.; Li, Q.-Q.; Fan, S.-S. Cross-Stacked Carbon Nanotube Sheets Uniformly Loaded with SnO_2 Nanoparticles: a Novel Binder-Free and High-Capacity Anode Material for Lithium-Ion Batteries. *Adv. Mater.* **2009**, *21*, 2299–2304.
45. Noerochim, L.; Wang, J.-Z.; Chou, S.-L.; Li, H.-J.; Liu, H.-K. SnO_2-Coated Multiwall Carbon Nanotube Composite Anode Materials for Rechargeable Lithium-Ion Batteries. *Electrochim. Acta* **2010**, *56*, 314–320.
46. Zhang, H.; Song, H.; Chen, X.; Zhou, J.; Zhang, H. Preparation and Electrochemical Performance of SnO_2@Carbon Nanotube Core−Shell Structure Composites as Anode Material for Lithium-Ion Batteries. *Electrochim. Acta* **2012**, *59*, 160–167.
47. Ahn, D.; Xiao, X.; Li, Y.; Sachdev, A. K.; Park, H. W.; Yu, A.; Chen, Z. Applying Functionalized Carbon Nanotubes to Enhance Electrochemical Performances of Tin Oxide Composite Electrodes for Li-Ion Battery. *J. Power Sources* **2012**, *212*, 66–72.
48. Shao, Q.-G.; Chen, W.-M.; Wang, Z.-H.; Qie, L.; Yuan, L.-X.; Zhang, W.-X.; Hu, X.-L.; Huang, Y.-H. SnO_2-Based Composite Coaxial Nanocables with Multi-Walled Carbon Nanotube and Polypyrrole as Anode Materials for Lithium-Ion Batteries. *Electrochem. Commun.* **2011**, *13*, 1431–1434.
49. Dhanabalan, A.; Yu, Y.; Li, X.; Chen, W.; Bechtold, K.; Gu, L.; Wang, C. Porous SnO_2/CNT Composite Anodes: Influence of Composition and Deposition Temperature on the Electrochemical Performance. *J. Mater. Res.* **2010**, *25*, 1554–1560.
50. Hu, R.; Sun, W.; Liu, H.; Zeng, M.; Zhu, M. The Fast Filling of Nano-SnO_2 in CNTs by Vacuum Absorption: a New Approach to Realize Cyclic Durable Anodes for Lithium Ion Batteries. *Nanoscale* **2013**, *5*, 11971–11979.
51. Guler, M. O.; Cevher, O.; Cetinkaya, T.; Tocoglu, U.; Akbulut, H. Nanocomposite Anodes for Lithium-Ion Batteries Based on SnO_2 on Multiwalled Carbon Nanotubes. *Int. J. Energy Res.* **2014**, *38*, 487–498.
52. An, G.; Na, N.; Zhang, X.; Miao, Z.; Miao, S.; Ding, K.; Liu, Z. SnO_2/Carbon Nanotube Nanocomposites Synthesized in Supercritical Fluids: Highly Efficient Materials for Use as a Chemical Sensor and as the Anode of a Lithium-Ion Battery. *Nanotechnology* **2007**, *18*, 435707.
53. Liu, H. Carbon Nanotubes Anchored with SnO_2 Nanosheets as Anode for Enhanced Li-Ion Storage. *J. Mater. Sci.: Mater. Electron.* **2014**, *25*, 3353–3357.
54. Fu, Y.; Ma, R.; Shu, Y.; Cao, Z.; Ma, X. Preparation and Characterization of SnO_2/Carbon Nanotube Composite for Lithium Ion Battery Applications. *Mater. Lett.* **2009**, *63*, 1946–1948.
55. Noerochim, L.; Wang, J.-Z.; Chou, S.-L.; Wexler, D.; Liu, H.-K. Free-Standing Single-Walled Carbon Nanotube/SnO_2 Anode Paper for Flexible Lithium-Ion Batteries. *Carbon* **2012**, *50*, 1289–1297.
56. Wepasnick, K. A. Surface and Structural Characterization of Multi-Walled Carbon Nanotubes Following Different Oxidative Treatments. *Carbon* **2011**, *49*, 24–36.
57. Choi, B. G.; Yang, M. H.; Hong, W. H.; Choi, J. W.; Huh, Y. S. 3D Macroporous Graphene Frameworks for Supercapacitors with High Energy and Power Densities. *ACS Nano* **2012**, *6*, 4020–4028.
58. Choi, S. H.; Ko, Y. N.; Lee, J.-K.; Kang, Y. C. 3D MoS_2−Graphene Microspheres Consisting of Multiple Nanospheres with Superior Sodium Ion Storage Properties. *Adv. Funct. Mater.* **2015**, *25*, 1780–1788.
59. Zhou, X.; Wan, L.-J.; Guo, Y.-G. Binding SnO_2 Nanocrystals in Nitrogen-Doped Graphene Sheets as Anode Materials for Lithium-Ion Batteries. *Adv. Mater.* **2013**, *25*, 2152–2157.
60. Okpalugo, T. I. T.; Papakonstantinou, P.; Murphy, H.; McLaughlin, J.; Brown, N. M. D. High Resolution XPS Characterization of Chemical Functionalized MWCNTs and SWCNTs. *Carbon* **2005**, *43*, 153–161.
61. Li, X.; Yu, Q.; Yu, C.; Huang, Y.; Li, R.; Wang, J.; Guo, F.; Zhang, Y.; Gao, S.; Zhao, L. Zinc-Doped SnO_2 Nanocrystals as Photoanode Materials for Highly Efficient Dye-Sensitized Solar Cells. *J. Mater. Chem. A* **2015**, *3*, 8076–8082.
62. Yang, Z.; Du, G.; Guo, Z.; Yu, X.; Li, S.; Chen, Z.; Chen, G.; Zhang, P.; Liu, H. K. Plum-Branch-Like Carbon Nanofibers Decorated with SnO_2 Nanocrystals. *Nanoscale* **2010**, *2*, 1011–1017.
63. Liu, C.-J.; Huang, H.; Cao, G.-Z.; Xue, F.-H.; Camacho, R. A. P.; Dong, X.-L. Enhanced Electrochemical Stability of Sn-Carbon Nanotube Nanocapsules as Lithium-Ion Battery Anode. *Electrochim. Acta* **2014**, *144*, 376–382.
64. Kim, H.; Zhang, J. K.; Choi, J.-M.; Song, M. S.; Park, J. H. Controlled Thermal Sintering of a Metal−Metal Oxide−Carbon Ternary Composite with a Multiscale Hollow Nanostructure for Use as an Anode Material in Li-Ion Batteries. *Chem. Commun.* **2014**, *50*, 2589–2591.
65. Kim, H.; Park, G. O.; Kim, Y.; Muhammad, S.; Yoo, J.; Balasubramanian, M.; Cho, Y.-H.; Kim, M.-G.; Lee, B.; Kang, K.; et al. New Insight into the Reaction Mechanism for Exceptional Capacity of Ordered Mesoporous SnO_2 Electrodes *via* Synchrotron-Based X-Ray Analysis. *Chem. Mater.* **2014**, *26*, 6361–6370.
66. Zhang, L.; Wu, H. B.; Liu, B.; Lou, X. W. Formation of Porous SnO_2 Microboxes ctive Leaching for Highly Reversible Lithium Storage. *Energy Environ. Sci.* **2014**, *7*, 1013–1017.
67. Ding, L.; He, S.; Miao, S.; Jorgensen, M. R.; Leubner, S.; Yan, C.; Hickey, S. G.; Eychmüller, A.; Xu, J.; Schmidt, O. G. Ultrasmall SnO_2 Nanocrystals: Hot-bubbling Synthesis, Encapsulation in Carbon Layers and Applications in High Capacity Li-Ion Storage. *Sci. Rep.* **2014**, *4*, 4647.
68. Sun, H.; Xin, G.; Hu, T.; Yu, M.; Shao, D.; Sun, X.; Lian, J. High-Rate Lithiation-Induced Reactivation of Mesoporous

Hollow Spheres for Long-Lived Lithium-Ion Batteries. *Nat. Commun.* **2014**, *5*, 4526.
69. Luo, J.; Liu, J.; Zeng, Z.; Ng, C. F.; Ma, L.; Zhang, H.; Lin, J.; Shen, Z.; Fan, H. J. Three-Dimensional Graphene Foam Supported Fe_3O_4 Lithium Battery Anodes with Long Cycle Life and High Rate Capability. *Nano Lett.* **2013**, *13*, 6136–6143.
70. Zhou, G.; Wang, D.-W.; Li, F.; Zhang, L.; Li, N.; Wu, Z.-S.; Wen, L.; Lu, G. Q.; Cheng, H.-M. Graphene-Wrapped Fe_3O_4 Anode Material with Improved Reversible Capacity and Cyclic Stability for Lithium Ion Batteries. *Chem. Mater.* **2010**, *22*, 5306–5313.
71. Gogotsi, Y.; Simon, P. True Performance Metrics in Electrochemical Energy Storage. *Science* **2011**, *334*, 917–918.
72. Obrovac, M. N.; Christensen, L.; Le, D. B.; Dahn, J. R. Alloy Design for Lithium-Ion Battery Anodes. *J. Electrochem. Soc.* **2007**, *154*, A849–A855.
73. Nitta, N.; Wu, F.; Lee, J. T.; Yushin, G. Li-ion Battery Materials: Present and Future. *Mater. Today* **2015**, *18*, 252–264.
74. Park, M.-S.; Kang, Y.-M.; Wang, G. X.; Dou, S.-X.; Liu, H.-K. The Effect of Morphological Modification on the Electrochemical Properties of SnO_2 Nanomaterials. *Adv. Funct. Mater.* **2008**, *18*, 455–461.
75. Choi, S. H.; Kang, Y. C. Yolk−Shell, Hollow, and Single-Crystalline $ZnCo_2O_4$ Powders: Preparation Using a Simple One-Pot Process and Application in Lithium-Ion Batteries. *ChemSusChem* **2013**, *6*, 2111–2116.
76. Zhu, Y.; Xu, Y.; Liu, Y.; Luo, C.; Wang, C. Comparison of Electrochemical Performances of Olivine $NaFePO_4$ in Sodium-Ion Batteries and Olivine $LiFePO_4$ in Lithium-Ion Batteries. *Nanoscale* **2013**, *5*, 780–787.
77. Ko, Y. N.; Park, S. B.; Jung, K. Y.; Kang, Y. C. One-Pot Facile Synthesis of Ant-Cave-Structured Metal Oxide−Carbon Microballs by Continuous Process for Use as Anode Materials in Li-Ion Batteries. *Nano Lett.* **2013**, *13*, 5462–5466.
78. Shi, Y.; Wang, J.-Z.; Chou, S.-L.; Wexler, D.; Li, H.-J.; Ozawa, K.; Liu, H.-K.; Wu, Y.-P. Hollow Structured Li_3VO_4 Wrapped with Graphene Nanosheets *vs* Prepared by a One-Pot Template-Free Method as an Anode for Lithium-Ion Batteries. *Nano Lett.* **2013**, *13*, 4715–4720.